Molecular basis of mRNA transport by a kinesin-1–atypical tropomyosin complex

Lyudmila Dimitrova-Paternoga,[1,2,3] Pravin Kumar Ankush Jagtap,[2] Anna Cyrklaff,[1] Vaishali,[1,4] Karine Lapouge,[5] Peter Sehr,[6] Kathryn Perez,[5] Simone Heber,[1] Christian Löw,[3] Janosch Hennig,[2] and Anne Ephrussi[1]

[1]Developmental Biology Unit, European Molecular Biology Laboratory (EMBL) Heidelberg, 69117 Heidelberg, Germany; [2]Structural and Computational Biology Unit, EMBL Heidelberg, 69117 Heidelberg, Germany; [3]Centre for Structural Systems Biology (CSSB), Deutsches Elektronen-Synchrotron (DESY), EMBL Hamburg, 22607 Hamburg, Germany; [4]Faculty of Biosciences, Heidelberg University, 69120 Heidelberg, Germany; [5]Protein Expression and Purification Core Facility, EMBL Heidelberg, 69117 Heidelberg, Germany; [6]Chemical Biology Core Facility, EMBL Heidelberg, 69117 Heidelberg, Germany

Kinesin-1 carries cargos including proteins, RNAs, vesicles, and pathogens over long distances within cells. The mechanochemical cycle of kinesins is well described, but how they establish cargo specificity is not fully understood. Transport of *oskar* mRNA to the posterior pole of the *Drosophila* oocyte is mediated by *Drosophila* kinesin-1, also called kinesin heavy chain (Khc), and a putative cargo adaptor, the atypical tropomyosin, *a*Tm1. How the proteins cooperate in mRNA transport is unknown. Here, we present the high-resolution crystal structure of a Khc–*a*Tm1 complex. The proteins form a tripartite coiled coil comprising two in-register Khc chains and one *a*Tm1 chain, in antiparallel orientation. We show that *a*Tm1 binds to an evolutionarily conserved cargo binding site on Khc, and mutational analysis confirms the importance of this interaction for mRNA transport in vivo. Furthermore, we demonstrate that Khc binds RNA directly and that it does so via its alternative cargo binding domain, which forms a positively charged joint surface with *a*Tm1, as well as through its adjacent auxiliary microtubule binding domain. Finally, we show that *a*Tm1 plays a stabilizing role in the interaction of Khc with RNA, which distinguishes *a*Tm1 from classical motor adaptors.

Intracellular transport is an essential cellular function that is ensured by a vast cytoskeletal network and three major classes of motor proteins, namely kinesins, dyneins, and myosins (Hirokawa et al. 2009; de Lanerolle 2012; Olenick and Holzbaur 2019). Whereas myosins are responsible for short-range transport along randomly oriented actin filaments, kinesins and dyneins provide long-range directional transport on a polarized microtubule network (Titus 2018). Kinesin-1, a microtubule plus end-directed motor, was the first kinesin identified and is well characterized (Vale et al. 1985; Hirokawa et al. 2009). It transports diverse cargos including proteins, organelles, mRNA nucleoprotein complexes (mRNPs), and viruses (Chudinova and Nadezhdina 2018; Garcin and Straube 2019; Banerjee et al. 2020) and is essential for numerous processes such as endoplasmic reticulum (ER)-Golgi transport, mitochondrial distribution in axons and dendrites, cell migration, and embryonic axis formation (Hirokawa et al. 2009).

Kinesin-1 harbors an N-terminal motor domain, followed by a long coiled-coil stalk that mediates homodimerization, and a flexible tail with regulatory function (Fig. 1A; Seeger and Rice 2013). The two motor domains are powered by ATP hydrolysis, which elicits conformational changes that allow the kinesin molecule to move processively along microtubules (Qin et al. 2020). The kinesin-1 stalk associates with cargos either directly or via adaptor proteins that bind to the C-terminal region of the domain (Cross and Dodding 2019). Although a large portion of kinesin-1 transport is mediated by the adaptor kinesin light chain (Klc), the transport of mRNA cargos such as mRNP granules in dendrites or *oskar* in the *Drosophila* oocyte appears to be independent of Klc (Diefenbach et al. 1998; Kanai et al. 2004; Loiseau et al. 2010; Cross and Dodding 2019).
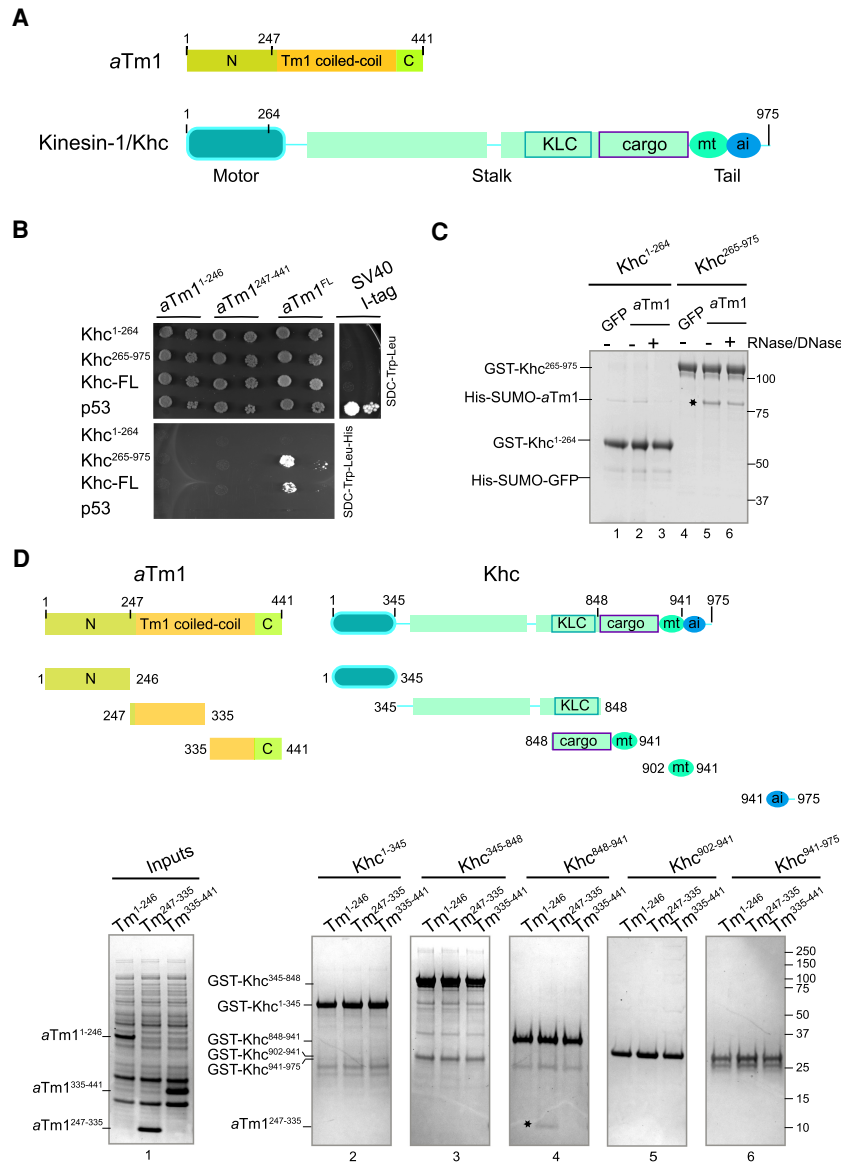
Figure 1. *a*Tm1 interacts with the alternative cargo binding domain of Khc. (*A*) Schematic representation of *a*Tm1 and kinesin heavy chain (Khc). *a*Tm1 has a central coiled-coil domain, flanked by mostly unstructured N- and C-terminal regions. Khc comprises an N-terminal motor-domain (amino acids 1–345), followed by a long coiled-coil stalk (amino acids 345–902) and an unstructured tail (amino acids 902–975). The stalk includes the kinesin light chain (Klc) binding region (amino acids 792–839) and an alternative cargo binding region (amino acids 848–902). The tail comprises an ATP-independent microtubule binding domain (amino acids 910–938) and an IAK (isoleucine-alanine-lysine) motif (amino acids 938–950), responsible for the autoinhibition of Khc (Williams et al. 2014). Although in many studies the alternative cargo binding region has been considered part of the tail, based on its structural and functional features, we categorize it as part of the coiled-coil stalk. (*B*) Yeast two-hybrid analysis shows that *a*Tm1 and Khc interact. The Khc variants were tagged with the GAL4 binding domain, and the *a*Tm1 variants were fused to the GAL4 activation domain. Yeast cells were cotransformed with different combinations of the above-mentioned constructs and spotted in two 10-fold dilutions on SDC–Leu–Trp and SDC–Leu–Trp–His plates. (*C*) A GST (glutathione S-transferase) pull-down assay reveals direct binding of *a*Tm1 to kinesin: GST-tagged Khc$^{1–264}$ and Khc$^{265–975}$ were immobilized on glutathione beads and mixed with *E.coli* lysates containing recombinantly expressed His$_6$-SUMO-*a*Tm1-FL and His$_6$-SUMO-GFP (Supplemental Fig S1A). The eluates were analyzed by SDS-PAGE. The asterisk indicates the interaction of *a*Tm1^{FL} with Khc$^{265–975}$. (*D*) *a*Tm1$^{247–335}$ interacts with the alternative cargo binding domain of Khc$^{848–941}$. In vitro binding of GST-tagged Khc truncations (schematic *top left*) to different *a*Tm1 truncations (schematic *top right*), premixed with *E.coli* whole-cell lysate. The asterisk indicates the interaction of *a*Tm1$^{247–334}$ with Khc$^{848–941}$.

In *Drosophila,* localization of *oskar* mRNA to the posterior pole of the developing oocyte drives abdominal patterning and germline formation in the embryo (Ephrussi and Lehmann 1992). The directional transport of RNA is mediated by both the dynein and kinesin transport machineries (Clark et al. 2007; Zimyanin et al. 2008). In the germline syncytium, the oocyte is transcriptionally quiescent and relies on mRNAs provided by 15 interconnected nurse cells for its growth and development (Roth and Lynch 2009). Upon transcription in the nurse cells, *oskar* mRNA is transported into the oocyte on the microtubule cytoskeleton by the minus end-directed dynein motor complex (Clark et al. 2007). Within the oocyte, the microtubule plus end-directed motor kinesin-1 or kinesin heavy chain (Khc) in *Drosophila* (Lawrence et al. 2004) trans-

ports *oskar* to the posterior pole where the mRNA is localized (for review, see Trcek and Lehmann 2019). *oskar* mRNA transport depends on a region of Khc downstream from the Klc binding site that includes an alternative cargo binding domain and an ATP-independent microtubule binding site (Williams et al. 2014).

Moreover, kinesin-mediated *oskar* transport requires a number of *cis* and *trans* factors. One of these factors is a unique isoform of the actin binding protein tropomyosin 1, known as Tm1-I/C, which we refer to here as atypical or *a*Tm1 for simplicity (Loiseau et al. 2010; Veeranan-Karmegam et al. 2016; Gáspár et al. 2017a). In the absence of *a*Tm1, *oskar* mRNA fails to localize to the posterior pole of the oocyte, as kinesin recruitment to *oskar* mRNA requires *a*Tm1 function (Erdélyi et al. 1995; Gáspár et al.

2017a). Furthermore, the fact that tethering of the Khc motor domain to *oskar* restores posterior localization of the mRNA in a *Tm1* protein-null background suggested that *a*Tm1 is an essential adaptor for Khc-mediated *oskar* transport (Gáspár et al. 2017a).

Here, we show that *a*Tm1 homodimers adopt an unusual antiparallel coiled-coil conformation. Moreover, *a*Tm1 binds to an alternative conserved cargo binding region in Khc, forming a tripartite coiled-coil complex with a positively charged surface. Finally, we show in vivo that the function of *a*Tm1 is ensured by its Khc interacting domain and that this atypical Tm1 functions in stabilizing the interaction of Khc with RNA rather than as a classical adaptor.

Results

*a*Tm1 binds to the alternative cargo binding site of Khc

It was previously reported that *a*Tm1 is necessary for the recruitment of Khc to *oskar* mRNA and that the two proteins physically interact (Veeranan-Karmegam et al. 2016; Gáspár et al. 2017a). To elucidate the molecular basis of the *a*Tm1-Khc interaction, we first performed a yeast two-hybrid analysis, which confirmed that *a*Tm1 (Tm1-FL) binds both full-length Khc (Khc-FL) and Khc$^{265-975}$ (Fig. 1B). Because the interaction of Khc and *a*Tm1 was formerly tested by coimmunoprecipitation (IP) experiments from S2 cells or *Drosophila* ovarian lysates, neither of which is performed in a nucleic acid-free environment (Veeranan-Karmegam et al. 2016; Gáspár et al. 2017a), we also probed the interaction by pull-down of recombinant Khc and *a*Tm1 proteins in the presence of DNase and RNase (Fig. 1C; inputs in Supplemental Fig. S1A). Binding of *a*Tm1 to Khc was preserved under these conditions (Fig. 1C, right panel, lanes 5,6), indicating the specific and direct interaction of *a*Tm1 with Khc.

To further narrow down the *a*Tm1 and Khc interacting regions, we performed GST pull-down assays on shorter fragments of the proteins (Fig. 1D; Supplemental Fig. S1B,C). This revealed that *a*Tm1$^{247-335}$ binds Khc$^{848-941}$ (Fig. 1D, panel 4), which comprises the alternative cargo binding region and the ATP-independent microtubule binding region of Khc (Fig. 1D; Seiler et al. 2000; Williams et al. 2014). Veeranan-Karmegam et al. (2016) have previously suggested that *a*Tm1 interacts with residues 914–936 of Khc. However, the fact that Khc$^{902-941}$ did not interact with *a*Tm1 in our assays (Fig. 1D, panel 5) indicates that *a*Tm1$^{247-335}$ binds to the conserved alternative cargo binding site of Khc (residues 848–902) (Supplemental Fig. S1D).

The alternative cargo binding region of Khc is essential for *oskar* mRNA localization

The alternative cargo binding region in Khc was originally identified in *Neurospora crassa* kinesin (Nkin), where deletion of this site abolished the ability of the protein to rescue the *Nkin* null mutant phenotype (Seiler et al. 2000). In *Drosophila*, deletion of the entire C terminus of Khc, which includes the alternative cargo binding region and the regulatory tail, also led to an *oskar* mRNA localization defect among others (Williams et al. 2014). To investigate the relevance of this cargo binding region for *oskar* mRNA transport, we expressed RNAi-resistant Khc-FL-mKate2 and Khc$^{855-911\Delta}$-mKate2 (wherein the cargo binding domain is deleted) fusion proteins in a *khc*-RNAi background (Fig. 2A; Supplemental Fig. S2). Khc$^{855-911\Delta}$ localized to the posterior pole of the oocyte (Fig. 2B, upper right panel), indicating that Khc motor function and polarity of the microtubule cytoskeleton were preserved. However, *oskar* mRNA failed to localize at the posterior pole (Fig. 2B, bottom right panel) and the eggs produced failed to hatch (Fig. 2C), demonstrating that the alternative cargo binding region of *Drosophila* Khc, and likely its interaction with *a*Tm1, play a major role in *oskar* mRNA transport.
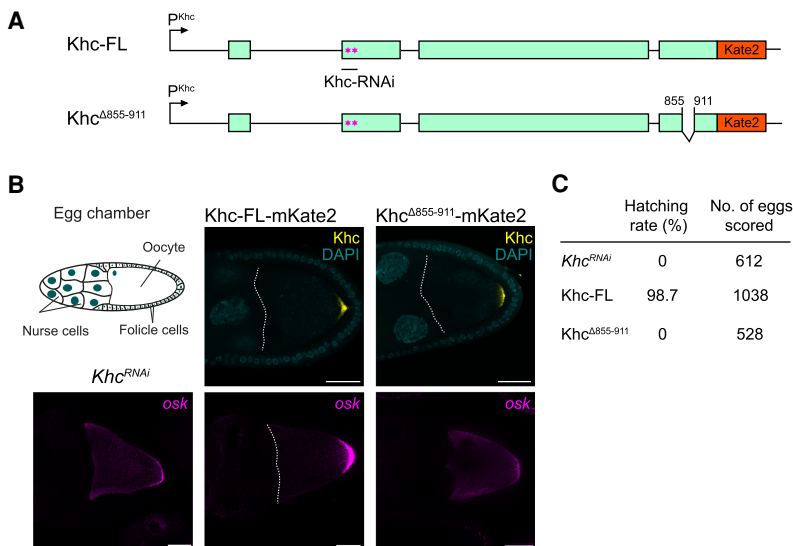

Figure 2. *oskar* mRNA localization depends on the alternative cargo binding domain of Khc. (*A*) Schematic of Khc-FL and Khc$^{\Delta855-911}$ transgenic constructs resistant to *khc*-RNAi used in this study. The pink stars indicate silent point mutations in the region targeted by *khc*-RNAi; Khc$^{\Delta855-911}$ lacks the alternative cargo binding domain. (*B*) Deletion of the alternative cargo binding region of Khc leads to *oskar* mRNA mislocalization. (*Top middle* and *right* panels) Khc-FL and Khc$^{\Delta855-911}$ variants tagged with mKate2 were expressed in a *khc*-RNAi background. Khc variants and *khc*-RNAi were expressed in the germline, which includes nurse cells and the oocyte (see schematic *top left*). (*Bottom* panels) *oskar* mRNA was visualized by single-molecule (sm)FISH. Scale bar, 25 μm. (*C*) Hatching rates of eggs from flies expressing Khc-FL or Khc$^{\Delta855-911}$ transgenes in Khc knockdown background.

The Khc interaction domain of aTm1 is essential for oskar *localization*

The region of aTm1 (residues 247–335) that interacts with Khc consists of a coiled coil that is also present in the classical Tm1-A isoform (residues 282–335), preceded by a unique N-terminal sequence predicted to be at least partially helical (Fig. 1D). To understand the functional significance of the aTm1–Khc interaction, we generated GFP-tagged aTm1 truncations in which the Khc interaction site was either present or absent and tested them in vivo. We expressed the constructs in $Tm1^{eg9}$ mutant flies, in which aTm1 is not present and oskar mRNA fails to localize at the posterior of the oocyte (Supplemental Fig. S3A–C, first panel; Erdélyi et al. 1995; Gáspár et al. 2017a).

Expression of transgenic full-length aTm1 (aTm1^{FL}) and aTm1$^{1–334}$ restored oskar localization to the posterior pole of $Tm1^{eg9}$ oocytes (Fig. 3A–C), suggesting that the aTm1 C-terminal region is nonessential for this function. Expression of the minimal Khc interaction region of aTm1 (aTm1$^{247–334}$) also promoted oskar localization in $Tm1^{eg9}$ oocytes. Although the RNA was not as concentrated at the posterior pole as upon aTm1^{FL} or aTm1$^{1–334}$ expression (Fig. 3B,C; analysis was performed as in Gaspar et al. 2014), the female progeny developed ovaries and were fertile. Neither aTm1$^{1–247}$ nor aTm1$^{335–441}$ could restore oskar localization in $Tm1^{eg9}$ oocytes (Supplemental

Fig. S3C). These data show that the core domain of aTm1 (residues 247–334) identified as the Khc binding domain is essential for oskar mRNA localization.

Interestingly, despite supporting oskar mRNA localization, GFP-aTm1$^{247–334}$, which lacks a major portion of the unique N-terminal region of aTm1, does not accumulate at the posterior pole of the oocyte, in contrast to aTm1^{FL} or aTm1$^{1–334}$. This suggests that the aTm1 N-terminal domain interacts with components of the pole plasm or with oskar mRNA itself, resulting in aTm1 accumulation at the oocyte posterior.

aTm1 coiled-coil dimers adopt an antiparallel configuration

To gain insight into the molecular basis of aTm1–Khc interaction, we used crystallography to determine the structure of aTm1 alone and in complex with Khc. The classical actin-binding tropomyosins (Tm1-PG and Tm1-PA in *Drosophila*) are highly conserved in eukaryotes (Fig. 4A), where they form long parallel coiled coils that polymerize in a head-to-tail fashion along the actin filaments (Parry and Squire 1973). Residues 81–165 of Tm1-PG are present in aTm1 whose coiled-coil region is further extended by 20 unique residues at the N terminus (aTm1$^{262–366}$) (Fig. 4A), which we included in our constructs.

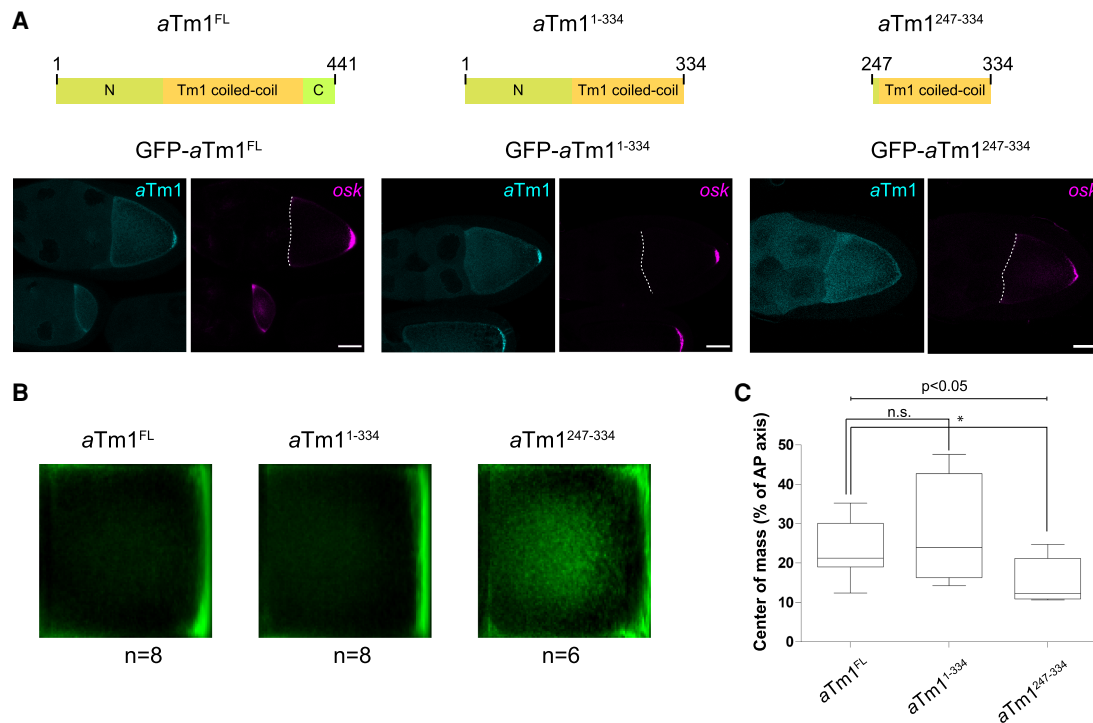We performed crystallization trials with different aTm1 truncations (Fig. 4A) and obtained crystals for

Figure 3. aTm1$^{247–334}$ rescues oskar mRNA localization in $Tm1^{eg9}/Tm1^{eg9}$ mutant. (*A*) Confocal images of $Tm1^{eg9}/Tm1^{eg9}$ egg chambers expressing GFP-tagged aTm1^{FL}, aTm1$^{1–334}$, and aTm1$^{247–334}$ variants. oskar mRNA was visualized by smFISH. Scale bar, 25 µm. (*B*) Mean oskar distribution (green) in stage 9 oocytes from the flies in *A*. *n* indicates the number of oocytes analyzed. (*C*) Position of oskar mRNA center of mass relative to the geometric center of the oocyte represented in box plots with minimum and maximum whiskers. The analysis was performed as in Gaspar et al. (2014).
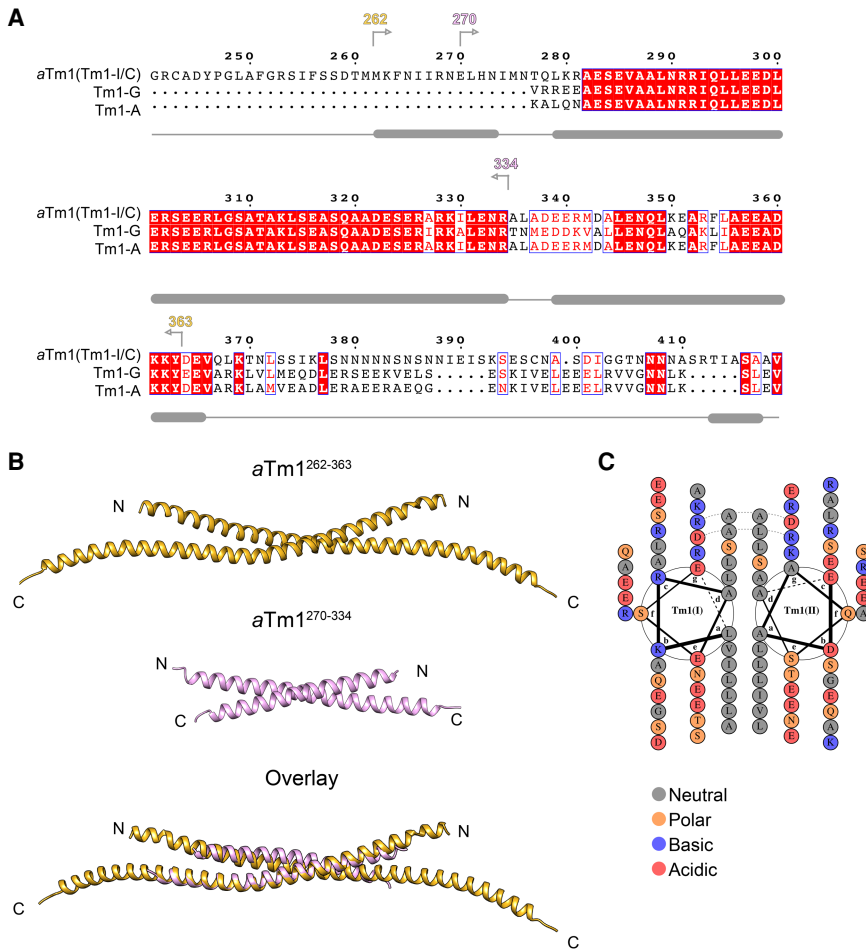
A

B

*a*Tm1²⁶²⁻³⁶³

*a*Tm1²⁷⁰⁻³³⁴

Overlay

C

- ● Neutral
- ● Polar
- ● Basic
- ● Acidic

Figure 4. *a*Tm1 forms an antiparallel coiled coil. (*A*) Multiple sequence alignment of three Tm1 isoforms from *Drosophila melanogaster*. The shared coiled-coil region of *a*Tm1 extends N-terminally into a unique predicted α helix (the predicted secondary structure is indicated under the alignment where regions with thick gray bars indicate α helices). Tm1-PG and Tm1-PA are two classical actin-binding nonmuscle isoforms that lack this N-terminal extension. The boundaries of the crystallized constructs of *a*Tm1 are indicated *above* the alignment. The alignment was done by ESPript 3 (Robert and Gouet 2014). (*B*) *a*Tm1 coiled-coil region crystallized in an antiparallel conformation. Crystal structures of *a*Tm1²⁶²⁻³⁶³ (*top* panel) and *a*Tm1²⁷⁰⁻³³⁴ (*middle* panel) and their superimposition (*bottom* panel). Residues 261–358 are resolved in the crystal structure of the *a*Tm1²⁶²⁻³⁶³ construct. Residues 277–319 in the first coil and residues 273–330 in the second coil are resolved in *a*Tm1²⁷⁰⁻³³⁴. (*C*) The coiled coil of *a*Tm1 is stabilized primarily by hydrophobic interactions. Helical wheel diagram of *a*Tm1²⁶²⁻³⁶³ as generated by DrawCoil 1.0 (https://grigoryanlab.org/drawcoil). The dashed lines connecting Arg292 and Asp299 indicate salt bridges between these residues.

*a*Tm1^{262–363} and *a*Tm1^{270–334} constructs that diffracted to a resolution of 2.45 Å and 2.3 Å, respectively (Fig. 4B). The structures were solved by ab initio molecular replacement with Ample and were refined to an R_{work}/R_{free} of 0.25/0.29 and of 0.23/0.27 for Tm1^{262–363} and Tm1^{270–334}, respectively (see Supplemental Table S1 for structural statistics; Bibby et al. 2012). Residues 261–358 were fitted into the density of the *a*Tm1^{262–363} crystal structure, whereas residues 277–319 in the first coil and residues 273–330 in the second coil were resolved in *a*Tm1^{270–334}.

Both truncations crystallized as antiparallel coiled coils with an average backbone RMSD of 1 Å between residues 278 and 328 (Fig. 4B). A helical wheel diagram of *a*Tm1^{262–363} in Figure 4C demonstrates that the two α helices are held together primarily by hydrophobic residues at the *a* and *d* positions of the heptad repeats, which is typical for coiled-coil structures. The interaction is additionally stabilized by two symmetric salt bridges on the surface from Arg292 and Asp299 of chain A to Asp299 and Arg292 of chain B, respectively.

The unusual antiparallel coiled-coil conformation of *a*Tm1 distinguishes it from the canonical Tm1 isoforms, which form parallel coiled coils, and might be an additional factor attributing to it specific functions.

*a*Tm1–Khc interaction domains form a triple coiled coil of two kinesin chains and one *a*Tm1 chain

We next reconstituted, biophysically characterized, and crystallized the minimal *a*Tm1–Khc complex. To do so, the initially identified protein boundaries (Fig. 1D) were further refined to improve protein solubility and yields, after which individually purified *a*Tm1^{252–334} and Khc^{855–941} were mixed and analyzed by gel filtration (Fig. 5A). Upon addition of *a*Tm1, the Khc peak shifted to a higher apparent molecular weight, indicating complex formation. Interestingly, the *a*Tm1 peak fractions shifted to a later retention time (larger elution volume) indicative of compaction of the protein in the complex upon binding (Fig. 5A, middle gel [lanes 7–9] and lower gel [lanes 8–10]). Also, although we mixed the proteins in a 1:1 ratio before injection onto the column (Fig. 5A, right panel, lowest gel, lane 1), the ratio of the bands in the complex peak (Fig. 5A, right panel, lowest gel, lanes 8–12), as well as the presence of an additional *a*Tm1 peak (Fig. 5A, right panel, lowest gel, lanes 3–7) indicate that Khc is in excess in the complex. To determine the affinity of the *a*Tm1–Khc interaction, we performed surface plasmon resonance (SPR) experiments using an anti-GST antibody

Figure 5. The *a*Tm1–Khc complex forms a tripartite coiled coil. (*A*) Reconstitution of an *a*Tm1–Khc complex, consisting of the minimal interaction regions of the two proteins (*left* schematic). Size exclusion chromatography (S200 resin) of Khc$^{855-941}$, *a*Tm1$^{252-334}$, and a 1:1 mixture of both proteins. The UV trace of *a*Tm1 alone could not be recorded because of the very low extinction coefficient of this truncation. Peak fractions were analyzed by gel electrophoresis in the *bottom* panel. (*B*) Binding of *a*Tm1$^{252-334}$ to Khc$^{848-941}$ analyzed by surface plasmon resonance (SPR). GST-tagged Khc$^{848-941}$ was used as a ligand, and increasing concentrations (indicated *above* the sensogram in nanomoles) of *a*Tm1 were added as analyte. Ligand to analyte was fitted using a standard 1:1 kinetic model with a $K_d = 141 \pm 6$ nM. (*C*) Crystal structure of the *a*Tm1$^{252-334}$/Khc$^{855-941}$ complex. Two different helical views (*left* panels) and the corresponding electrostatic views (*right* panels) are presented. The two Khc chains (aquamarine) are parallel and in register, whereas the single *a*Tm1 chain (gold) is in an antiparallel conformation. The crystal structures consist of *a*Tm1 (residues 259–324), KhcI (residues 855–923), and KhcII (residues 855–916). The *bottom* two *left* and *right* panels represent ribbon and electrostatic views of *a*Tm1$^{262-363}$ for comparison. (*D*) The triple coiled coil of the *a*Tm1–Khc complex is stabilized primarily by hydrophobic interactions; helical wheel diagram generated by DrawCoil 1.0 (https://grigoryanlab.org/drawcoil).

coated chip allowing immobilization of GST-Khc[848–941]. aTm1[252–334] was added stepwise (fivefold increasing concentration at each step), and the resulting sensorgram could be fitted to a standard 1:1 kinetic model with a dissociation constant (K_d) of 141 ± 6 nM (Fig. 5B).

The aTm1[252–334]–Khc[855–942] complex crystallized in a P2$_1$ space group. A data set was collected to a resolution of 2.3 Å and a model obtained by ab initio molecular replacement with Arcimboldo (Rodríguez et al. 2009). The structure was refined to a final R_{work}/R_{free} of 0.24/0.28, incorporating aTm1 (residues 259–324), KhcI (residues 855–923), and KhcII (residues 855–916) in 1:2 (aTm1:Khc) stoichiometry (Fig. 5C). The trimeric structure comprises two parallel, in-register Khc chains and a single, antiparallel Tm1 chain, with the Khc C-terminal residues in close proximity to the aTm1 N-terminal region. This arrangement suggests that the coiled coil of aTm1 opens to accommodate the coiled-coil stalk of Khc. A possible explanation for the mechanism of aTm1–Khc complex formation would be a lower dimerization propensity of the aTm1 homotypic coiled coil. To estimate the K_d of the aTm1 homodimer, we performed an isothermal titration calorimetry (ITC) experiment whereby we fitted the heat changes upon dilution of aTm1[252–334] (Supplemental Fig. S4A), and obtained a K_d of 10 μM. Thus, aTm1 has a higher affinity to Khc (K_d in the nanomolar range) (Fig. 5B) than to another aTm1, which explains why aTm1 forms a complex with the Khc homodimer.

Superimposition of the aTm1 homodimer on the Khc–aTm1 complex structure revealed no major changes of the aTm1 helix except for a kink caused by the looping out of T277 (Supplemental Fig. S4B). As crystals of Khc truncations were only obtained in the presence of aTm1, we could not evaluate the effect of aTm1 binding on Khc conformation.

The triple coiled coil is held together by van der Waals forces between mostly hydrophobic residues at "a" and "d" positions of each helix (Fig. 5D). Additionally, the surface of the complex is characterized by a positively charged patch, not present in the aTm1[262–363] homodimer, formed by the polar side chains of K884, K887, and R888 of Khc (Fig. 5C, right panels), important for RNA binding (see below).

Mutational analysis of a*Tm1–Khc interaction contacts*

To verify the interaction surface of aTm1 and Khc, we generated single point mutants that would be expected to disrupt complex formation. We first mutated two amino acid residues in the unique region of the aTm1 coiled coil, L271 at the hydrophobic core of the complex, and Q278, whose polar side chain is positioned near the hydrophobic core due to a kink in aTm1 (Supplemental Figs. S4B, S5A). Mutating aTm1 L271 to the smaller nonpolar residue alanine or the bulkier, charged arginine only mildly affected the interaction with Khc, whereas the Q278A mutation had no effect (Supplemental Fig. S5B, left and middle panels). This might be due to the extensive hydrophobic core of the aTm1–Khc complex. To achieve disruption of the interaction, we designed two triple mutants—

aTm1[I267A/L271A/L279A] (aTm1[T1]) at the unique N-terminal extension of aTm1, and aTm1[L296A/L300A/L307A] (aTm1[T2]) in the middle of the aTm1 coiled coil—and a combination of the two (aTm1[Hexa]) (Fig. 6A; Supplemental Fig. S5C). Both the aTm1[T1] and aTm1[Hexa] mutations fully abolished interaction with Khc, as determined by in vitro binding assays (Supplemental Fig. S5D). However, although we changed the target residues to alanines in order to preserve the helical propensity of aTm1, circular dichroism (CD) spectroscopy showed that the mutations affected substantially the structure of the aTm1 homodimers (Supplemental Fig. S5E).

As the triple mutant T2 showed residual binding to Khc, we focused on T1 and designed two double mutants, aTm1[I267A/L271A] (aTm1[D1]) and aTm1[L271A/L279A] (aTm1[D2]) (Fig. 6A). The mutations introduced in aTm1[D2] substantially reduced the solubility of aTm1[252–334] since most of the recombinantly expressed protein precipitated after centrifugation of the $E.coli$ lysate (Fig. 6B). This might be due to the fact that L279 lies at the junction of the two aTm1 chains in close proximity to L314 and A321 of the second chain and is therefore essential for the stability of the aTm1 coiled coil. This again demonstrates how the fact that aTm1 uses the same surface to form a homodimer and to interact with Khc renders it difficult to generate an aTm1 mutant that has no effect on the structure of aTm1 yet disrupts its interaction with Khc. Thus, even the two mutations in aTm1[D1] appear to destabilize the coiled coil to some extent, as a SEC-MALS (size exclusion chromatography multiangle light scattering) measurement indicates that aTm1[D1] behaves as a mixture of dimers and monomers (Supplemental Fig. S5F). Nonetheless, the aTm1[D1] mutations did not affect solubility of the protein and had only a moderate effect on its secondary structure as assessed by CD spectroscopy (Fig. 6B,C). More importantly, aTm1[D1] interaction with Khc was notably reduced in our GST pull-down assays and as evaluated by SPR (Fig. 6D; Supplemental Fig. S5G).

To assess aTm1[D1] function in vivo, we generated a GFP-tagged aTm1[D1] transgene and tested its ability to rescue $oskar$ mRNA localization in $tm1^{eg1}$ oocytes. smFISH revealed that the bulk of $oskar$ mRNA was unlocalized, with only trace amounts detected at the posterior pole (Fig. 6E; Supplemental Fig. S5H), further confirming the importance of the aTm1–Khc interaction for $oskar$ mRNA transport.

a*Tm1 stabilizes the interaction of Khc with RNA*

Previous findings suggest a direct interaction of aTm1 with the $oskar$ 3′ UTR, supporting the notion that aTm1 might function as a Khc adaptor for RNA (Gáspár et al. 2017a). We therefore tested whether aTm1 interacts with poly (U) RNA in vitro. Considering the rescue of the $Tm1^{eg9/eg9}$ loss-of-function mutant by aTm1[1–334] (Fig. 3), we focused our analysis on this portion of the protein. Since recombinantly expressed aTm1[1–335] was unstable and gave rise to two proteolytic products (Supplemental Fig. S6A), we generated further truncations of aTm1 to
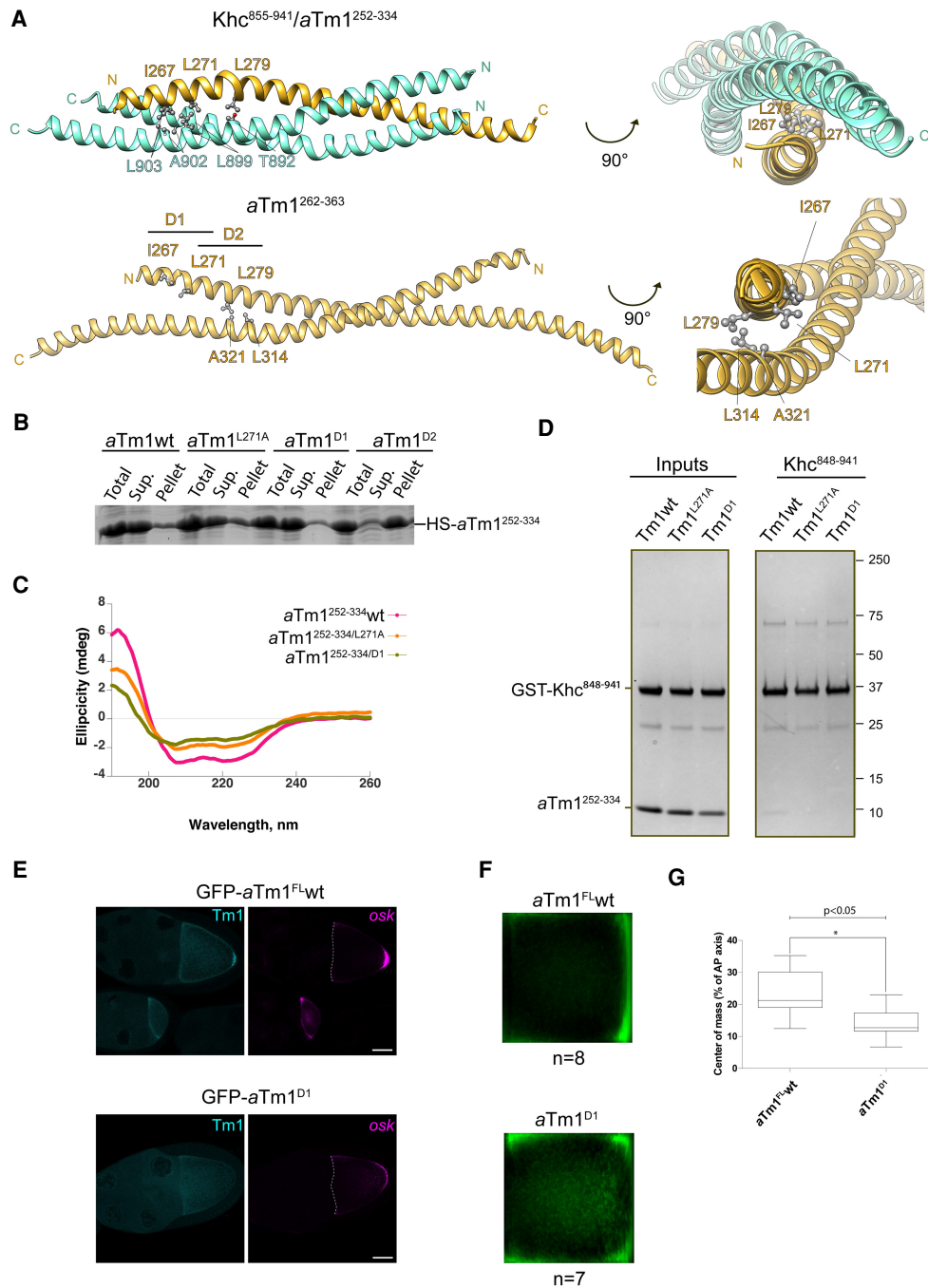
Figure 6. Mutational analysis of the aTm1–Khc interaction. (A) Designing double point mutations at the hydrophobic core of aTm1–Khc coiled coil. Ribbon views of aTm1–Khc complex (*top* panels) or aTm1 homodimer (*bottom* panels) in two different orientations. Three residues—I267, L271, and L279—at the hydrophobic core of the trimeric complex are highlighted. In aTm1[D1], residues I267 and L271 are mutated to alanine. In aTm1[D2], residues L271 and L279 are mutated to alanine. (B) aTm1[D2] has significantly reduced solubility. Total, supernatant, and pellet fractions of *E. coli* lysate with recombinantly expressed His-SUMO tagged aTm1[252–334] wild-type and mutant variants were analyzed on SDS-PAGE and stained with Coomassie. (C) aTm1[D1] has the characteristic coiled-coil fold. (Magenta) CD analysis of aTm1wt, (orange) aTm1[L271A], (green) aTm1[D1]. (D) aTm1[D1] mutation causes strong reduction of the interaction with Khc. Pull-down assays of GST-tagged Khc[848–942] with different variants of aTm1[252–334]. (*Left* panel) Purified aTm1 variants were mixed in excess with Khc[848–942], immobilized on GSH beads. (*Right* panel) After incubation and extensive washing, the eluates were analyzed on SDS-PAGE and stained with Coomassie. (E) Tm1[D1] causes *oskar* mRNA localization defects in vivo. (*Left* panels) Egg chambers (stage 9) from flies expressing GFP-aTm1-FL and GFP-aTm1[D1] in the *Tm1[eg9]/Tm1[eg9]* background. (*Right* panels) *oskar* mRNA was detected by smFISH. Scale bar, 25 µm. (F) Mean *oskar* distribution (green) in stage 9 oocytes from the flies in *E*. *n* corresponds to the number of analyzed oocytes. (G) Position of *oskar* mRNA center of mass relative to the geometric center of the oocyte, represented in box plot with minimum and maximum whiskers. GFP-aTm1[FL] wt panels and quantification in *E–G* are the same as in Figure 3.

probe its interaction with RNA. Previously we showed by NMR, which allows detection of stable as well as transient interactions, that Tm1$^{1-246}$, which encompasses most of the low complexity N-terminal region of aTm1, interacts directly with U$_{25}$ RNA (Vaishali et al. 2021). Moreover, electrophoretic mobility shift assays (EMSAs) showed that the C-terminal region of aTm1$^{1-334}$, Tm1$^{252-334}$, binds oligo-(U$_{25}$) only weakly, with a K_d >10 µM, as compared with Tm1$^{54-335}$, which demonstrated significantly higher affinity for RNA (Fig. 7A). These findings suggest that a major RNA binding activity of aTm1 lies within the N-domain (residues 1–246).

As deletion of the N domain of aTm1 had only a mild effect on *oskar* localization (Fig. 3; Supplemental Fig. S3), we suspected the presence of an additional RNA binding moiety within the Khc–aTm1 complex. Indeed, as mentioned above, the structure of the aTm1–Khc complex displays a joint positively charged surface (Fig. 5C). We therefore performed EMSAs with Khc$^{855-941}$ alone or in complex with aTm1. Khc on its own bound RNA with high affinity (high nanomolar range) and, at higher concentrations, appeared to form oligomers with RNA that failed to enter the gel (Fig. 7B). Upon addition of Tm1$^{252-334}$ or Tm1$^{54-335}$ to Khc in a 1:2 ratio, the affinity increased and the protein–RNA complexes could be resolved (Fig. 7B). The affinity increase for Tm1$^{54-335}$, as expected, has a stronger effect, as the N domain contributes to RNA binding. As an independent method to assess the interaction of aTm1–Khc with RNA, we performed filter binding assays, which overall confirmed the EMSA results showing that the interaction of Khc with RNA in solution is enhanced almost to the same extent by Tm1$^{252-334}$ and Tm1$^{54-334}$ (Fig. 7C). Together, these data show that aTm1 prevents formation of Khc–RNA aggregates and that the aTm1 and Khc synergize in RNA binding.

To ascertain that the interaction of Khc with RNA is not due to stickiness of the Khc$^{855-941}$ truncation, we also performed EMSAs with the full-length Khc, alone or in the presence of Tm1$^{252-334}$ or Tm1$^{54-335}$. This confirmed that Khc-FL binds to RNA and that its affinity for RNA increases when aTm1 is present (Supplemental Fig. S6B).

The Khc$^{855-941}$ fragment used in our RNA binding and crystallization experiments contains both the aTm1 binding site (residues 855–909) and the ATP-independent microtubule binding site (AMB, residues 910–938). To determine which of the two regions mediates RNA binding, we tested two further truncations from which the AMB was either partially or fully deleted (Khc$^{855-920}$ and Khc$^{855-909}$). Both proteins, and especially Khc$^{855-909}$, showed reduced binding to RNA (Supplemental Fig. S6C). To test for involvement of the positively charged patch on the surface of aTm1–Khc in RNA binding, we mutated Lys884, Lys887, and Arg888 of Khc to alanines (Khc$^{855-941/TA}$) (Supplemental Fig. S6D). This reduced the binding of Khc to RNA but had no effect on protein folding as measured by CD spectroscopy or on binding to aTm1 as assessed by a GST pull-down assay (Supplemental Fig. S6E–G). These experiments show that both the aTm1 binding site and the AMB contribute to RNA binding, most likely by formation of an extended RNA in-

teraction surface. These data are consistent with the finding of Williams et al. (2014) that Khc$^{1-910}$, which lacks the auxiliary microtubule binding domain, does not support *oskar* mRNA localization.

Taken together, our findings demonstrate that Khc can bind RNA directly and that aTm1 acts in stabilizing rather than in mediating the Khc–RNA interaction, distinguishing aTm1 from a classical kinesin adaptor.

Discussion

In recent decades, mechanisms of mRNA transport and the composition of mRNP transport complexes have been extensively studied, yet only a few adaptor proteins linking RNAs to the transport machineries have been identified. These include She2p/She3p for myosin-based RNA transport in *S. cerevisiae* (Takizawa and Vale 2000), and Egalitarian/BicD proteins for dynein-based transport in *Drosophila* (Dienstbier and Li 2009; Dienstbier et al. 2009). The atypical tropomyosin isoform aTm1 was recently proposed to function as an adaptor for Khc-mediated transport of *oskar* mRNA in *Drosophila* (Veeranan-Karmegam et al. 2016; Gáspár et al. 2017a). Classical Tm1 isoforms form parallel coiled coils that polymerize in head-to-tail fashion along actin filaments and are known to regulate different functions of the actin cytoskeleton (Parry and Squire 1973; Gunning et al. 2015). aTm1, which is present in Drosophilidae, has a shortened coiled-coil region flanked on both sides by unique, intrinsically disordered N-terminal and C-terminal sequences. Crystal structures of the aTm1 coiled coil presented in this study reveal an antiparallel conformation with a coiled-coil region extended by 20 amino acids beyond the conserved region (Fig. 4). Coiled coils play vital roles in nearly all biological processes and are among the most studied structural motifs (Truebestein and Leonard 2016). A few point mutations in the hydrophobic core are sufficient to cause a switch in the orientation of the coiled coil or the number of coils involved in the interaction (Mason and Arndt 2004; Malashkevich et al. 2015). Therefore, it is likely that the unique extension of the aTm1 coiled-coil region causes the antiparallel topology of the two chains. Importantly, two point mutations in this region have a dramatic effect on aTm1's interaction with Khc, which suggests that the unique sequence contributes to defining the specificity of aTm1 for Khc, both at the secondary and tertiary structure level (Fig. 6). Additionally, the switched orientation of the aTm1 coiled coil prevents interaction of the protein with actin and thus prevent its interference with the function of the classical actin-binding tropomyosin isoforms (Cho et al. 2016).

Although we could not determine a structure of the Khc dimer on its own, we assume that its conformation does not change significantly when bound to aTm1. This is corroborated by rotary shadowing negative stain EM images of Khc, which show that the motor domains are symmetrically attached to a long rod, a conformation that can be achieved only when Khc is a parallel in-register coiled coil (Hirokawa et al. 1989). The aTm1 homodimeric
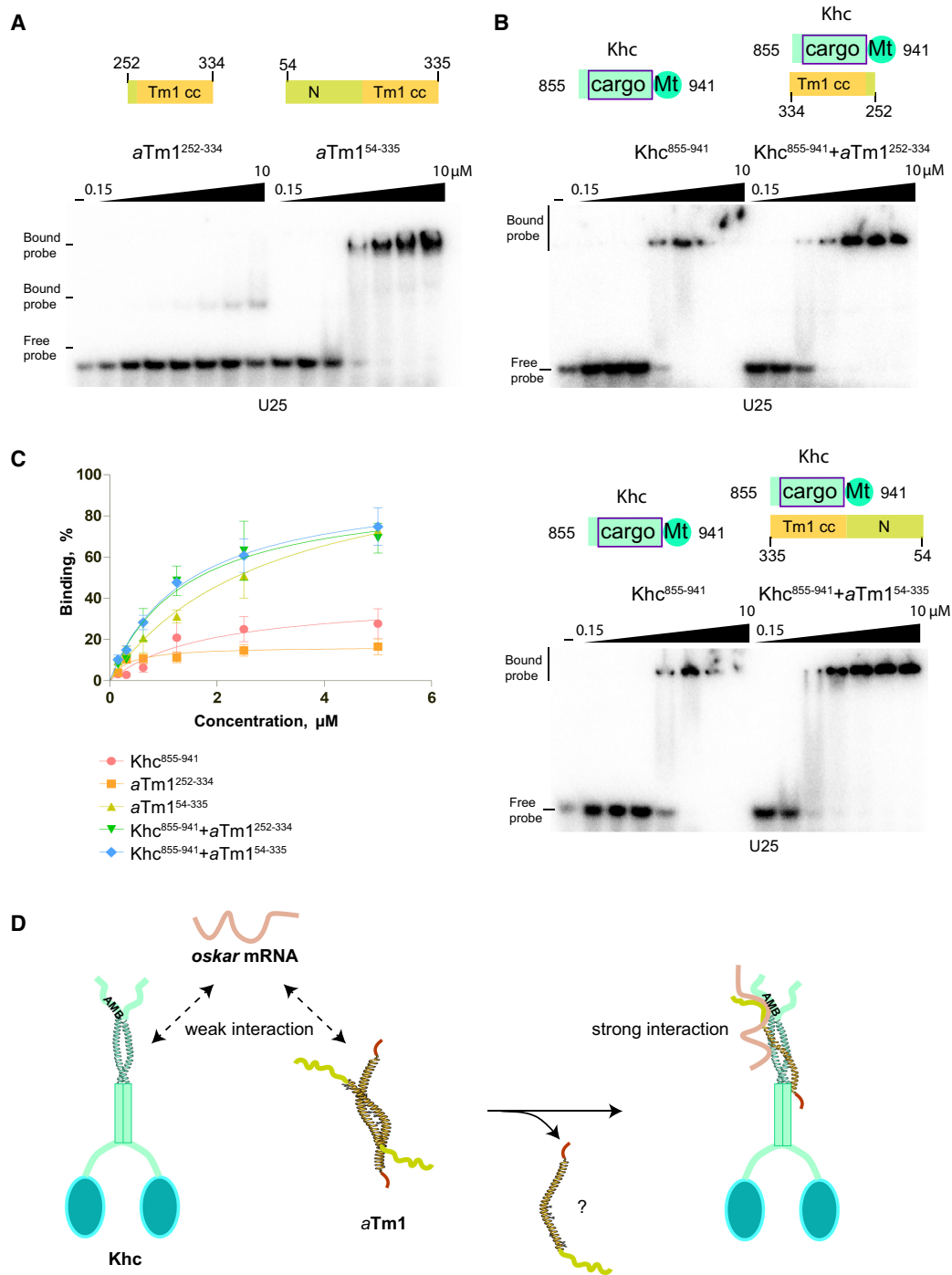
Figure 7. *a*Tm1 as a kinesin modulator. (*A*) *a*Tm1-N domain binds to RNA. Electrophoretic mobility shift assay (EMSA) of *a*Tm1$^{252–334}$ and *a*Tm1$^{54–335}$ variants. ^{32}P-labeled oligo-(U$_{25}$) was incubated with twofold increasing concentrations (0.15, 0.3 ….10 µM) of recombinantly purified proteins in 15-µL reactions as indicated. The samples were then loaded on 6% native gel and visualized by autoradiography. Free probe was run in the first lane. (*B*) Khc binds to RNA alone and better in the presence of *a*Tm1. Electrophoretic mobility shift assay (EMSA) of Khc$^{855–942}$ alone and in the presence of *a*Tm1$^{252–334}$ (*left* gel) or of *a*Tm1$^{54–335}$ (*right* gel). For the complex, *a*Tm1 was added to Khc in 1:2 molar ratio prior to performing serial dilutions. (*C*) Nitrocellulose filter binding assay of *a*Tm1 and Khc variants alone and in complex. ^{32}P-labeled oligo-(U$_{25}$) probe was incubated with increasing concentrations of proteins and protein complexes. The mixture was then passed through a nitrocellulose filter, and the radioactive probe left on the filter was measured as a fraction of the total probe that was added to the reaction. (*D*) Hypothetical model of *a*Tm1 as a modulator of Khc interaction with RNA. *a*Tm1 and Khc each bind RNA weakly on their own. To accommodate the Khc coiled coil, the *a*Tm1 homodimer opens, allowing formation of a tripartite coiled coil composed of one *a*Tm1 and two Khc chains. The second *a*Tm1 might be rearranged and promote formation of higher order structures. Binding of *a*Tm1 to Khc might elicit conformational changes in Khc or, alternatively, stabilize the Khc RNA binding surface and thus allow the Khc-*a*Tm1 complex to interact with higher affinity and/or specificity with RNA. Since the region with which Khc interacts with RNA incorporates both the alternative cargo binding domain and the adjacent auxiliary microtubule binding domain, the binding of *a*Tm1 to Khc might regulate the kinetic activity of Khc.

coiled coil, on the other hand, must open to allow binding to the kinesin homodimer, thus posing the question of what happens to the second *a*Tm1 chain (Fig. 7D). It might form an individual complex with another Khc homodimer or, alternatively, rearrange such that it remains bound to the portion of the *a*Tm1 coiled coil not in complex with Khc. This arrangement can further provide a platform for the formation of higher-order structures.

The interaction of Tm1 with Khc involves the alternative cargo binding region of Khc, which lies immediately downstream from the Klc binding domain (Fig. 1). This region was initially identified as cargo binding in the fungus *N. crassa* and was subsequently shown to be the major binding site for other adaptors and their respective cargos (Diefenbach et al. 2002, 2004; Setou et al. 2002; Kanai et al. 2004; Glater et al. 2006). We have shown that deletion of this region in *Drosophila* Khc results in *oskar* mislocalization and female sterility (Fig. 2), a phenotype more severe than that of complete loss of *a*Tm1, in which case the eggs still hatch and develop into adult sterile flies. This suggests that the alternative cargo binding region of Khc might have functions beyond *oskar* mRNA localization also in *Drosophila*. For example, it has been shown that the mitochondrial adaptor Milton binds also to the alternative cargo binding domain, suggesting that in Khc$^{\Delta855-911}$ mitochondrial transport to and within the oocyte might also be affected (Cox and Spradling 2006). Moreover, Milton along with SNAP25, which is an adaptor for vesicular transport, and the ribosome receptor p180 appear to bind Khc also via coiled-coil interactions, suggesting a binding mechanism similar to the *a*Tm1–Khc interaction described here (Diefenbach et al. 2002, 2004; Glater et al. 2006; Randall et al. 2013).

Functionally, coiled coils allow the formation of long rigid structures, especially when they involve more than two chains, and they may play the role of "molecular rulers," spacing the different functional regions of a protein (Truebestein and Leonard 2016). Thus, with the Klc binding site and the alterative cargo binding region adjacent to one another and potentially prone to steric hindrance, the coiled-coil structure might provide space for the simultaneous binding of cargos to these two regions. It will be interesting in the future to determine whether different cargos can indeed be cotransported by a single Khc molecule.

Retrograde transport by different kinesins along microtubules comprises a major fraction of the intracellular transport of mRNP granules. Surprisingly however, there are to date scarce mechanistic details of how the cargo might be recognized and how it can be attached to Khc. Only recently, the transport of β-actin and β2B-tubulin mRNAs was reconstituted in vitro, whereby APC (adenomatous polyposis coli) links the mRNAs to kinesin-2 through the cargo adaptor KAP3 (Baumann et al. 2020). Another study suggests that the transport of some axonal mRNPs depends on KLC1, which also implies a more classical adaptor-based transport mechanism (Fukuda et al. 2021). Here, we have shown that the N domain (residues 1–246) of *a*Tm1 binds RNA, whereas the region immediately adjacent to it (residues 247–334) interacts with the alternative cargo binding

region of Khc (Figs. 1, 7). Therefore, it is appealing to imagine *a*Tm1 as an adaptor for Khc as well. However, deletion of the N domain in vivo resulted in only minor *oskar* mRNA mislocalization, and sole expression of the Khc binding domain almost restored fully the accumulation of *oskar* at the posterior pole of the oocyte (Fig. 3). As demonstrated, Khc binds to RNA also on its own, and its RNA affinity increases in the presence of *a*Tm1 (Fig. 7). Moreover, the Khc-RNA interaction appears to be mediated by both the *a*Tm1 binding surface and the adjacent ATP-independent microtubule binding region (Supplemental Fig. S6). This explains the strong effect of deletion of the ATP-independent microtubule binding region on *oskar* mRNA localization (Williams et al. 2014). Therefore, *a*Tm1 appears to act as a stabilizer of the Khc interaction with RNA rather than as a classical adaptor (Fig. 7).

It is possible that *a*Tm1, upon binding, induces a conformation change of Khc, leading to increased RNA binding. This is supported by the structure reported here, as part of the AMB site of Khc appears to acquire a helical conformation (resides 909–920), although predicted to be disordered. Despite the lack of an isolated Khc structure for comparison, it can be speculated that the binding of *a*Tm1 stabilizes the helical conformation of the alternative cargo binding domain that extends into the AMB site and thus enables a higher-affinity interaction of Khc with RNA. Interestingly, downstream from AMB (residues 938–950) (Williams et al. 2014) is the Khc IAK autoinhibitory motif, which interacts with the motor domain of Khc and keeps the protein inactive in the absence of cargo (Kaan et al. 2011). Because of the antiparallel topology of the *a*Tm1 chain within the *a*Tm1–Khc complex, the N domain of *a*Tm1 is in proximity to the IAK motif of Khc. Thus, besides enabling the binding of cargo to Khc, *a*Tm1 might also play a role in release of the autoinhibited conformation of Khc. This might explain the observation that, upon deletion of the N domain of *a*Tm1, most but not all *oskar* localizes to the oocyte posterior pole (Fig. 3; Supplemental Fig. S3).

Our high-resolution structure of the atypical Tm1 (*a*Tm1) suggests that the unique antiparallel coiled-coil conformation of its dimers might underlie the specific functions of this isoform. Together with our high-resolution structure of the complex of *a*Tm1 with Khc, our findings show that *a*Tm1 stabilizes the interaction of Khc with RNA. Whether *a*Tm1 binding increases Khc's specificity for *oskar* mRNPs alone or through additional protein-protein or protein-RNA interactions in vivo remains to be investigated. Future identification of the *a*Tm1 interactome and of the *oskar* mRNA sequence or structure to which the *a*Tm1–Khc complex binds will be essential to elucidate the full mechanism whereby this RNA transport complex recognizes its different cargos.

Materials and methods

Plasmid construction

Cloning techniques including digestion, ligation, and DNA electrophoresis were performed essentially as described in Sambrook

et al. (1989) unless indicated otherwise. Mutagenesis was performed according to Liu and Naismith (2008). All GST-tagged Khc constructs (Khc$^{1–264}$, Khc$^{265–975}$, Khc$^{1–345}$, Khc$^{345–848}$, Khc$^{848–941}$, Khc$^{941–975}$, Khc$^{902–941}$, Khc$^{559–941}$, Khc$^{623–941}$, and Khc$^{786–941}$) were cloned between BamHI and EcoRI sites of the pGEX6p-1 vector (Amersham). All His$_6$-SUMO tagged Tm1 (Tm1-FL, Tm1$^{1–335}$, Tm1$^{247–378}$, Tm1$^{1–246}$, Tm1$^{247–334}$, and Tm1$^{335–441}$) and Khc (Khc$^{855–941}$, Khc$^{855–909}$, and Khc$^{855–920}$) truncations were cloned between BamHI and SacI sites of the pETM11-His$_6$-SUMO plasmid (derived from pBR322, H. Besir, Protein Expression and Purification Core Facility, EMBL Heidelberg). The simple modular architecture research tool (SMART) was used for designing the truncation boundaries (Letunic and Bork 2018).

For yeast two-hybrid assays, Khc-FL, Khc$^{265–975}$, and Khc$^{265–975}$ were cloned between NdeI and BamHI sites of the pG4BDN22 vector, whereas Tm1-FL, Tm1$^{1–247}$, and Tm1$^{247–441}$ were cloned between NdeI and BamHI sites of the pG4ADHAN111 vector (Thoms et al. 2015).

The Tm1 integrase constructs were based on pUASp2-emGFP-Tm1RI (Gáspár et al. 2017a). Essentially, the aTm1 open reading frame (ORF) and 3′ UTR were cloned between BamHI and BglII sites of the pUASp vector (Rørth 1998). emGFP was inserted downstream from the pUAS promoter in-frame with the Tm1 coding sequence. To generate pUASp-attB-ΔK10-Tm1 constructs, the region of pUASp2-emGFP-Tm1 containing the pUAS promoter, emGFP, Tm1-FL, or truncations' ORFs, and Tm1 3′ UTR region were PCR-amplified and inserted between NotI and XbaI sites of pUASp-attB-ΔK10 plasmid using In-Fusion cloning according to the manufacturer's instructions (Takara).

To generate the pKhcp-attB-ΔK10-Khc-FL construct, we amplified the 2R:16266960–16273471 region from fly genomic DNA and inserted it between Eco147I and BamHI sites of pUASp-attB-ΔK10 vector, removing the pUAS promoter. We then performed site-directed mutagenesis using the following oligos: 5′-GTCT ACCTGTTTGATAAAGTCTTCAAACCGAATGCATC-3′ (fwd) and 5′-TTTATCAAACAGGTAGACCTTGCCCTGCAGACGA TG-3′ (rev) to change the region targeted by Khc-RNAi (Bloomington Stock 35409). The mKate2 coding sequence was added in-frame at the C terminus of the Khc ORF using the ligation-free cloning approach. To generate the pUASp-attB-ΔK10-Khc$^{Δ855–911}$ truncation, we performed inverse PCR with oligos starting at the boundaries of the truncation, followed by ligation of the product and transformation in E.coli.

Khc-FL was cloned with a HisSUMO-SNAP-tag between BamHI and HindIII sites of the pFastBacDual vector. All plasmids used in this study are summarized in Supplemental Table S2.

Protein expression and purification

GST- and His$_6$-SUMO-tagged proteins were expressed in BL21-CodonPlus(DE3)-RIL cells (Stratagene) by isopropyl β-D-1-thiogalactopyranoside (IPTG) induction for 16 h at 18°C. Cells were grown in Luria-Bertani (LB) medium (0.5% [w/v] yeast extract [MP], 1% [w/v] tryptone [MP], 0.5% [w/v] NaCl at pH 7.2) supplemented with antibiotics (100 µg/mL ampicillin or 10 µg/mL kanamycin and 34 µg/mL chloramphenicol). After harvesting, the pellets were lysed by a microfluidizer processor (Microfluidics) in 500 mM NaCl, 20 mM Tris-HCl (pH 7.5), 5% glycerol, 0.01% NP-40, and 40 mM imidazole (only in the case of His$_6$-tagged proteins) buffer supplemented with protease inhibitor cocktail (Roche) and 5 mM β-mercaptoethanol. The lysates were subsequently cleared by centrifugation at 18,000 rpm for 20 min.

For GST-tagged proteins, the lysates were incubated with gluthatione sepharose 4B (GE Healthcare) for 1 h at 4°C. After washing, the beads were directly used for binding assays (see below).

His$_6$-SUMO tagged proteins were affinity-purified by a His TRAP Ni column (GE Healthcare) and eluted over an imidazole gradient (40–600 mM). After cleavage of the tag by Senp2 protease, the proteins were passed one more time over a His TRAP Ni column to remove the tag and protease. Finally, the eluates were further separated on a Superdex 200 16/600 column in a 20 mM Tris-HCl (pH 7.5), 150 mM NaCl, and 0.5 mM TCEP buffer for crystallization and binding assays and 20 mM HEPES-Na (pH 7.5), 150 mM NaCl, and 0.5 mM TCEP for surface plasmon resonance (SPR) and CD spectroscopy.

His$_6$-SUMO-SNAP-tagged Khc-FL was expressed in 1 L of SF-21 insect cells at 1×10^6 cells/mL shaking culture infected with 10 mL of P1 virus stock. After expression for 3 d at 27.5°C, cells were harvested by centrifugation at 1000g for 20 min at 4°C. The pellet was lysed in a dounce tissue grinder in lysis buffer (20 mM Tris/HCl at pH 7.5, 500 mM NaCl, 1 mM MgCl$_2$, 0.1 mM ATP, 2 mM DTT, 5% glycerol, 0.2% Tween-20). The lysate was cleared by centrifugation and the soluble protein fraction was affinity-purified on a HisTrap Excel column (GE Healthcare). After elution in a 0–300 mM imidazole gradient, the HisSUMO-SNAP-fusion tag was cleaved by 3C protease digest upon dialysis in 25 mM HEPES/KOH (pH 7.3), 150 mM KCl, 1 mM MgCl$_2$, 0.1 mM ATP, and 2 mM DTT for 16 h before further purification by anion exchange chromatography on a HiTrap Q HP column (GE Healthcare), followed by size exclusion chromatography (SEC) on a Superdex 200 10/300 Increase column (GE Healthcare).

For expression of seleno-methionine (SeMet)-labeled Tm1$^{252–334}$, we used the B834(DE3) methionine auxotrophic E. coli strain. After transformation, the cells were grown in minimal M9 medium containing 50 µg/mL methionine overnight at 37°C. The bacteria were then scaled up to the volume of the expression culture and grown to OD$_{600}$ = 1 in minimal medium supplemented with methionine. The cells were then harvested, resuspended in minimal medium without methionine, and starved for 4–8 h before the addition of 50 µg/mL SeMet to the culture. After 30 min, protein expression was induced with 200 mM IPTG for 16 h at 18°C (for a detailed protocol see https://www .embl.de/pepcore/pepcore_services/protein_expression/ecoli/ seleno).

Yeast two-hybrid assay

The yeast two-hybrid analysis was performed according to James et al. (1996). The yeast two-hybrid strain PJ69-4a was transformed with the indicated aTm1 or Khc fragments cloned in pAS or pG4ADHAN vectors (Clontech Laboratories, Inc.), and plated on SDC–TRP–LEU or SDC–TRP–LEU–HIS plates. A positive interaction was monitored by growth on SDC–TRP–LEU–HIS plates. pTD1-1 (Clontech Laboratories, Inc.), which contains pGAL4-AD SV40 large T-antigen, and pVA3-1 (Clontech Laboratories, Inc.), which contains pGAL4-BD-tagged murine p53, were used as positive controls.

GST pull-down assays

Proteins for pull-down assays were purified in 20 mM Tris-HCl (pH 7.5), 150 mM NaCl, 5% glycerol, and 0.01% NP-40 binding buffer. Baits were purified on gluthatione sepharose beads (see above). Lysates from E. coli expressing the protein of interest, E. coli lysates mixed with prepurified bait proteins or pure proteins were added with bait protein five times in excess of the prey protein, immobilized on GSH beads. After incubation on a turning wheel at 4°C and extensive washing, the proteins were eluted in sample buffer (200 mM Tris-HCl at pH 6.8, 8% [w/v] SDS, 40% glycerol, 0.4% bromophenol blue, 100 mM DTT) for

30 sec at 90°C. The eluates were analyzed by SDS-PAGE and stained with Coomassie.

Crystallization, data collection, and structure determination

Tm1$^{262–363}$ was concentrated to 36 mg/mL and mixed in 1:1 ratio (100 nL:100 nL) with 0.1 M Tris-HCl (pH 8) and 40% MPD reservoir solution at 20°C. Rod-shaped crystals were obtained by sitting drop vapor diffusion method between day 21 and 35. Crystals were harvested in mother liquor without additional cryoprotectant. Tm1$^{270–334}$ produced needle-like crystals 1 d after setting the hanging drops at 20 mg/mL in 1:1 ratio with 0.1 M NH$_4$Ac (pH 4.6) and 15% (w/v) PEG 4000 reservoir solution. The crystals were harvested in mother liquor supplemented with 25% glycerol.

Tm1$^{252–334}$/Khc$^{855–942}$ complex crystals were obtained after mixing the SeMet-labeled Tm1$^{252–334}$ and unlabeled Khc$^{855–942}$ proteins in 1:1 ratio followed by further purification by size exclusion chromatography. The peak fractions corresponding to the complex were concentrated to 4.5 mg/mL and mixed in 1:1 ratio (100 nL:100 nL) with 0.2 M NaAc, 20% PEG 3350. Thin plate-shaped crystals were obtained after 1 d, and crystals were harvested in mother liquor supplemented with 25% glycerol.

Diffraction data sets were recorded at ID-29 beamline at the European Synchrotron Radiation Facility (ESRF), Grenoble, France. Data were processed with XDS (Kabsch 2010), and the structures were solved by ab initio molecular replacement with Ample (Bibby et al. 2012) or Archimboldo (Rodríguez et al. 2009). Model building and several cycles of refinement were performed with Coot (Emsley et al. 2010) and with the Phenix suite (Liebschner et al. 2019), respectively.

The crystal structures are deposited at the Protein Data Bank under the following accession codes: Tm1$^{262–363}$ (7BJG), Tm1$^{270–334}$ (7BJN), and Tm1$^{252–334}$/Khc$^{855–942}$ complex (7BJS).

Circular dichroism spectroscopy

The proteins were purified in 20 mM HEPES/NaOH (pH 7.5), 150 mM NaCl, and 0.5 mM TCEP for circular dichroism (CD) spectroscopy. Prior to measurement, the salt was diluted to 50 mM NaCl. The measurements were performed at a 20 μM concentration in a 0.2-mm cuvette at 20°C using a Jasco J-815 CD spectrometer. The monitored wavelength range was from 240 to 190 nm in 0.1-nm steps with an average of five points per wavelength. The data was plotted using GraphPad Prism 5.

Surface plasmon resonance (SPR)

Surface plasmon resonance (SPR) measurements were conducted using a BIAcore T200 instrument (GE Healthcare) in 20 mM HEPES-Na, pH 7.5, 150 mM NaCl, 0.5 mM TCEP, 0.005% Tween20, and 0.05% BSA at 25°C. Anti-GST antibody from the GST Capture kit was covalently immobilized to a CM5 sensor chip according to the supplier's instructions (GE Healthcare), and GST-tagged Khc$^{848–941}$ or GST were site-directed affinity-captured to the sample and reference flow cell, respectively. The binding of Tm1$^{252–334}$ at 15.625, 62.5, 250, 1000, and 4000 nM was measured in a single cycle kinetic with 90 sec injections and a final dissociation for 600 sec at a flow rate of 30 μL/min. The interaction was analyzed either as steady state affinity or by a kinetic fit of the sensorgrams using a 1:1 binding model.

Size exclusion chromatography multiangle light scattering (SEC-MALS)

One-hundred microliters of Tm1 WT or Tm1 D1 (2.0 mg/mL) was injected onto a Superdex 200 10/300 GL gel filtration column

(Cytiva) in 10 mM HEPES (pH 7.5), 150 mM NaCl, and 5 mM TCEP buffer at room temperature. The column was coupled to a MALS system (MiniDAWN and Optilab, Wyatt Technology). Data were analyzed using the Astra 7 software (Wyatt Technology). Measurements were performed in triplicate.

Isothermal titration calorimetry (ITC)

Experiments were performed using a Microcal PEAQ-ITC (Malvern Instrument GmbH). The protein was dialyzed overnight at 4°C against the ITC buffer (20 mM HEPES at pH 7.5, 150 mM NaCl, 5 mM TCEP). The Tm1 WT protein in the syringe, at a concentration of 1 mM, was injected into the cell containing the buffer. Titrations were performed at 20°C or 25°C and consisted of 13 or 25 injections. The data were fitted using the dissociation fitting model of the MicroCal PEAQ-ITC analysis software (Malvern).

Fly stocks and husbandry

Tm1 and Khc transgenic flies were generated by site-specific integration of the respective pUASp-attB-ΔK10 or pKhcp-attB-ΔK10 constructs (see above) with Φc31 integrase in VK18 (vas-phi-ZH2A, PBac(y[+]-attP-9A)VK00018, Bellen laboratory) fly line. emGFP-Tm1-FL, truncations, and point mutations were driven by one copy of oskGal4 ((Telley et al. 2012); FBtp0083699) in the Tm1^{eg9}/Tm1^{eg9} background (FBal0049223) (Erdélyi et al. 1995). Khc-FL-mKate2 and Khc$^{855–911Δ}$-mKate2 were constitutively expressed by the Khc endogenous promoter in the UASp-Khc RNAi Trip Line GL00330 (Staller et al. 2013) background where the expression of Khc-RNAi was driven by oskGal4.

All fly stocks were grown at 21°C–25°C in vials on standard cornmeal agar. Prior to dissection, freshly hatched flies were fed with dried yeast for 1–2 d.

Single-molecule fluorescent in situ hybridization (smFISH)

Forty-two probes against the oskar mRNA coding region and 3′ UTR were labeled with Atto633 according to Gáspár et al. (2017b). smFISH was performed essentially as in Gáspár et al. (2017a). In short, two to three pairs of Drosophila ovaries were fixed with 2% (v/v) PFA and 0.05% (v/v) Triton X-100 in PBS (pH 7.4) for 20 min on an orbital shaker, followed by two washes with PBT (PBS + 0.1% [v/v] Triton X-100 at pH 7.4) for 10 min each. Ovaries were then prehybridized in 100 μL of hybridization buffer (300 mM NaCl, 30 mM sodium citrate at pH 7.0, 15% [v/v] ethylene carbonate, 1 mM EDTA, 50 μg/mL heparin, 100 μg/mL salmon sperm DNA, 1% [v/v] Triton X-100) for 30 min at 42°C, to which 100 μL of probe mixture (25 nM per individual oligonucleotide in hybridization buffer) was added for an additional 2–3 h at 42°C. After hybridization, the following washes were carried out to remove excess probes: hybridization buffer, hybridization buffer to PBT in a 1:1 mixture, PBT (10 min at 42°C each), and PBT at room temperature. The samples were then mounted in 80% (v/v) 2,2-thiodiethanol (TDE) in PBS and viewed using a Leica TCS SP8 confocal microscope with a 63× 1.4 NA objective. To detect GFP-tagged Tm1 variants, the native fluorescence of GFP was visualized. Because the mKate2 tag was not visible after smFISH, we imaged the ovaries directly after fixation in 2% PFA/PBT for 20 min. The images were analyzed in ImageJ/Fiji. Analysis of the oskar mRNA center of mass distribution was performed according to Gáspár et al. (2014) and plotted with GraphPad Prism 5.

Immunological techniques

For Western blots, dissected ovaries were lysed in 2× SDS sample buffer (100 mM Tris-HCl at pH 6.8, 4% [w/v] SDS, 20% glycerol,

0.2% bromophenol blue, 50 mM DTT) by manual grinding and heated for 10 min at 85°C. After separation by SDS-PAGE, the lysates were blotted on Immobilon-P PVDF membrane (Millipore) by wet blot transfer for 2 h at 4°C and 80 V. After blocking in 5% milk/PBS-Tween, incubation with primary antibody for 16 h and secondary horse radish peroxidase (HPR)-conjugated antibody for 1 h, the blot was developed with Immobilon Western chemiluminiscent HPR substrate (Millipore).

The anti-Khc antibody was raised against the Khc$^{345–559}$ truncation in rabbits.

Electrophoretic mobility shift assays (EMSAs)

The U$_{25}$ RNA synthetic probe (IDT) was 5′ end-labeled with ATP, [γ-^{32}P] (Hartmann Analytic) using T4 polynucleotide kinase (Thermo Fisher) and subsequently purified using Illustra microspin G25 columns (GE Healthcare). Recombinant Tm1 or/and Khc truncations (concentrations indicated in the figure legends) were mixed with 2.5 nM probe in 20 mM Tris-HCl (pH 7.5), 150 mM NaCl, 5% glycerol, and 0.5 mM TCEP binding buffer in 15-µL reactions and incubated for 45 min on ice. The samples were subsequently separated on 6% native 0.5× TBE polyacrylamide gel for 1 h at 100 V. The gel was then dried and exposed overnight to a storage phosphor screen (GE), which was visualized with a Typhoon Trio Imager (GE Healthcare).

Filter binding assays

For the filter binding assays, 2 CPS/µL (counts per second) radiolabeled probe was mixed with protein or protein mixture in a 100-µL reaction volume. After incubation for 45 min on ice, the mixture was filtered through Whatman 0.45-µm pore size nitrocellulose filters. Only protein-RNA complexes were retained on the filters and detected by scintillation counting. Data fits were performed with GraphPad Prism 5 using a single site saturation binding mode.

Competing interest statement

The authors declare no competing interests.

References

Banerjee A, Kulkarni S, Mukherjee A. 2020. Herpes simplex virus: the hostile guest that takes over your home. *Front Microbiol* **11:** 733. doi:10.3389/fmicb.2020.00733

Baumann S, Komissarov A, Gili M, Ruprecht V, Wieser S, Maurer SP. 2020. A reconstituted mammalian APC-kinesin complex selectively transports defined packages of axonal mRNAs. *Sci Adv* **6:** eaaz1588. doi:10.1126/sciadv.aaz1588

Bibby J, Keegan RM, Mayans O, Winn MD, Rigden DJ. 2012. AMPLE: a cluster-and-truncate approach to solve the crystal structures of small proteins using rapidly computed ab initio models. *Acta Crystallogr D Biol Crystallogr* **68:** 1622–1631. doi:10.1107/S0907444912039194

Cho A, Kato M, Whitwam T, Kim JH, Montell DJ. 2016. An atypical Tropomyosin in *Drosophila* with intermediate filament-like properties. *Cell Rep* **16:** 928–938. doi:10.1016/j.celrep.2016.06.054

Chudinova EM, Nadezhdina ES. 2018. Interactions between the translation machinery and microtubules. *Biochemistry (Mosc)* **83:** S176–s189. doi:10.1134/S0006297918140146

Clark A, Meignin C, Davis I. 2007. A dynein-dependent shortcut rapidly delivers axis determination transcripts into the *Drosophila* oocyte. *Development* **134:** 1955–1965. doi:10.1242/dev.02832

Cox RT, Spradling AC. 2006. Milton controls the early acquisition of mitochondria by *Drosophila* oocytes. *Development* **133:** 3371–3377. doi:10.1242/dev.02514

Cross JA, Dodding MP. 2019. Motor-cargo adaptors at the organelle-cytoskeleton interface. *Curr Opin Cell Biol* **59:** 16–23. doi:10.1016/j.ceb.2019.02.010

de Lanerolle P. 2012. Nuclear actin and myosins at a glance. *J Cell Sci* **125:** 4945–4949. doi:10.1242/jcs.099754

Diefenbach RJ, Mackay JP, Armati PJ, Cunningham AL. 1998. The C-terminal region of the stalk domain of ubiquitous human kinesin heavy chain contains the binding site for kinesin light chain. *Biochemistry* **37:** 16663–16670. doi:10.1021/bi981163r

Diefenbach RJ, Diefenbach E, Douglas MW, Cunningham AL. 2002. The heavy chain of conventional kinesin interacts with the SNARE proteins SNAP25 and SNAP23. *Biochemistry* **41:** 14906–14915. doi:10.1021/bi026417u

Diefenbach RJ, Diefenbach E, Douglas MW, Cunningham AL. 2004. The ribosome receptor, p180, interacts with kinesin heavy chain, KIF5B. *Biochem Biophys Res Commun* **319:** 987–992. doi:10.1016/j.bbrc.2004.05.069

Dienstbier M, Li X. 2009. Bicaudal-D and its role in cargo sorting by microtubule-based motors. *Biochem Soc Trans* **37:** 1066–1071. doi:10.1042/BST0371066

Dienstbier M, Boehl F, Li X, Bullock SL. 2009. Egalitarian is a selective RNA-binding protein linking mRNA localization signals to the dynein motor. *Genes Dev* **23:** 1546–1558. doi:10.1101/gad.531009

Emsley P, Lohkamp B, Scott WG, Cowtan K. 2010. Features and development of *Coot. Acta Crystallogr D Biol Crystallogr* **66:** 486–501. doi:10.1107/S0907444910007493

Ephrussi A, Lehmann R. 1992. Induction of germ cell formation by oskar. *Nature* **358:** 387–392. doi:10.1038/358387a0

Erdélyi M, Michon AM, Guichet A, Glotzer JB, Ephrussi A. 1995. Requirement for *Drosophila* cytoplasmic tropomyosin in oskar mRNA localization. *Nature* **377:** 524–527. doi:10.1038/377524a0

Fukuda Y, Pazyra-Murphy MF, Silagi ES, Tasdemir-Yilmaz OE, Li Y, Rose L, Yeoh ZC, Vangos NE, Geffken EA, Seo HS, et al. 2021. Binding and transport of SFPQ-RNA granules by KIF5A/KLC1 motors promotes axon survival. *J Cell Biol* **220:** e202005051. doi:10.1083/jcb.202005051

Garcin C, Straube A. 2019. Microtubules in cell migration. *Essays Biochem* **63:** 509–520. doi:10.1042/EBC20190016

Gáspár I, Yu YV, Cotton SL, Kim DH, Ephrussi A, Welte MA. 2014. Klar ensures thermal robustness of oskar localization by restraining RNP motility. *J Cell Biol* **206:** 199–215. doi:10.1083/jcb.201310010

Gáspár I, Sysoev V, Komissarov A, Ephrussi A. 2017a. An RNA-binding atypical tropomyosin recruits kinesin-1 dynamically to *oskar* mRNPs. *EMBO J* **36:** 319–333. doi:10.15252/embj.201696038

Gáspár I, Wippich F, Ephrussi A. 2017b. Enzymatic production of single-molecule FISH and RNA capture probes. *RNA* **23:** 1582–1591. doi:10.1261/rna.061184.117

Glater EE, Megeath LJ, Stowers RS, Schwarz TL. 2006. Axonal transport of mitochondria requires milton to recruit kinesin heavy chain and is light chain independent. *J Cell Biol* **173:** 545–557. doi:10.1083/jcb.200601067

Gunning PW, Hardeman EC, Lappalainen P, Mulvihill DP. 2015. Tropomyosin—master regulator of actin filament function in the cytoskeleton. *J Cell Sci* **128:** 2965–2974.

Hirokawa N, Pfister KK, Yorifuji H, Wagner MC, Brady ST, Bloom GS. 1989. Submolecular domains of bovine brain kinesin identified by electron microscopy and monoclonal antibody decoration. *Cell* **56:** 867–878. doi:10.1016/0092-8674(89)90691-0

Hirokawa N, Noda Y, Tanaka Y, Niwa S. 2009. Kinesin superfamily motor proteins and intracellular transport. *Nat Rev Mol Cell Biol* **10:** 682–696. doi:10.1038/nrm2774

James P, Halladay J, Craig EA. 1996. Genomic libraries and a host strain designed for highly efficient two-hybrid selection in yeast. *Genetics* **144:** 1425–1436. doi:10.1093/genetics/144.4.1425

Kaan HY, Hackney DD, Kozielski F. 2011. The structure of the kinesin-1 motor-tail complex reveals the mechanism of auto-inhibition. *Science* **333:** 883–885. doi:10.1126/science.1204824

Kabsch W. 2010. XDS. *Acta Crystallogr D Biol Crystallogr* **66:** 125–132. doi:10.1107/S0907444909047337

Kanai Y, Dohmae N, Hirokawa N. 2004. Kinesin transports RNA: isolation and characterization of an RNA-transporting granule. *Neuron* **43:** 513–525. doi:10.1016/j.neuron.2004.07.022

Lawrence CJ, Dawe RK, Christie KR, Cleveland DW, Dawson SC, Endow SA, Goldstein LS, Goodson HV, Hirokawa N, Howard J, et al. 2004. A standardized kinesin nomenclature. *J Cell Biol* **167:** 19–22. doi:10.1083/jcb.200408113

Letunic I, Bork P. 2018. 20 years of the SMART protein domain annotation resource. *Nucleic Acids Res* **46:** D493–D496. doi:10.1093/nar/gkx922

Liebschner D, Afonine PV, Baker ML, Bunkóczi G, Chen VB, Croll TI, Hintze B, Hung LW, Jain S, McCoy AJ, et al. 2019. Macromolecular structure determination using X-rays, neutrons and electrons: recent developments in *Phenix. Acta Crystallogr D Struct Biol* **75:** 861–877. doi:10.1107/S2059798319011471

Liu H, Naismith JH. 2008. An efficient one-step site-directed deletion, insertion, single and multiple-site plasmid mutagenesis protocol. *BMC Biotechnol* **8:** 91. doi:10.1186/1472-6750-8-91

Loiseau P, Davies T, Williams LS, Mishima M, Palacios IM. 2010. *Drosophila* PAT1 is required for kinesin-1 to transport cargo and to maximize its motility. *Development* **137:** 2763–2772. doi:10.1242/dev.048108

Malashkevich VN, Higgins CD, Almo SC, Lai JR. 2015. A switch from parallel to antiparallel strand orientation in a coiled-coil X-ray structure via two core hydrophobic mutations. *Biopolymers* **104:** 178–185. doi:10.1002/bip.22631

Mason JM, Arndt KM. 2004. Coiled coil domains: stability, specificity, and biological implications. *Chembiochem* **5:** 170–176. doi:10.1002/cbic.200300781

Olenick MA, Holzbaur ELF. 2019. Dynein activators and adaptors at a glance. *J Cell Sci* **132.** doi:10.1242/jcs.227132

Parry DA, Squire JM. 1973. Structural role of tropomyosin in muscle regulation: analysis of the x-ray diffraction patterns from relaxed and contracting muscles. *J Mol Biol* **75:** 33–55. doi:10.1016/0022-2836(73)90527-5

Qin J, Zhang H, Geng Y, Ji Q. 2020. How kinesin-1 utilize the energy of nucleotide: the conformational changes and mechanochemical coupling in the unidirectional motion of kinesin-1. *Int J Mol Sci* **21:** 6977. doi:10.3390/ijms21186977

Randall TS, Moores C, Stephenson FA. 2013. Delineation of the TRAK binding regions of the kinesin-1 motor proteins. *FEBS Lett* **587:** 3763–3769. doi:10.1016/j.febslet.2013.09.049

Robert X, Gouet P. 2014. Deciphering key features in protein structures with the new ENDscript server. *Nucleic Acids Res* **42:** W320–W324. doi:10.1093/nar/gku316

Rodríguez DD, Grosse C, Himmel S, González C, de Ilarduya IM, Becker S, Sheldrick GM, Usón I. 2009. Crystallographic ab initio protein structure solution below atomic resolution. *Nat Methods* **6:** 651–653. doi:10.1038/nmeth.1365

Rørth P. 1998. Gal4 in the *Drosophila* female germline. *Mech Dev* **78:** 113–118. doi:10.1016/S0925-4773(98)00157-9

Roth S, Lynch JA. 2009. Symmetry breaking during *Drosophila* oogenesis. *Cold Spring Harb Perspect Biol* **1:** a001891. doi:10.1101/cshperspect.a001891

Sambrook J, Fritsch EF, Maniatis T. 1989. *Molecular cloning: a laboratory manual.* Cold Spring Harbor Laboratory Press, Cold Spring Harbor, NY.

Seeger MA, Rice SE. 2013. Intrinsic disorder in the kinesin superfamily. *Biophys Rev* **5:** 233–247. doi:10.1007/s12551-012-0096-5

Seiler S, Kirchner J, Horn C, Kallipolitou A, Woehlke G, Schliwa M. 2000. Cargo binding and regulatory sites in the tail of fungal conventional kinesin. *Nat Cell Biol* **2:** 333–338. doi:10.1038/35014022

Setou M, Seog DH, Tanaka Y, Kanai Y, Takei Y, Kawagishi M, Hirokawa N. 2002. Glutamate-receptor-interacting protein GRIP1 directly steers kinesin to dendrites. *Nature* **417:** 83–87. doi:10.1038/nature743

Staller MV, Yan D, Randklev S, Bragdon MD, Wunderlich ZB, Tao R, Perkins LA, Depace AH, Perrimon N. 2013. Depleting

gene activities in early *Drosophila* embryos with the 'maternal-Gal4-shRNA' system. *Genetics* **193:** 51–61. doi:10.1534/genetics.112.144915

Takizawa PA, Vale RD. 2000. The myosin motor, Myo4p, binds Ash1 mRNA via the adapter protein, She3p. *Proc Natl Acad Sci* **97:** 5273–5278. doi:10.1073/pnas.080585897

Telley IA, Gáspár I, Ephrussi A, Surrey T. 2012. Aster migration determines the length scale of nuclear separation in the *Drosophila* syncytial embryo. *J Cell Biol* **197:** 887–895. doi:10.1083/jcb.201204019

Thoms M, Thomson E, Baßler J, Gnädig M, Griesel S, Hurt E. 2015. The exosome is recruited to RNA substrates through specific adaptor proteins. *Cell* **162:** 1029–1038. doi:10.1016/j.cell.2015.07.060

Titus MA. 2018. Myosin-driven intracellular transport. *Cold Spring Harb Perspect Biol* **10:** a021972. doi:10.1101/cshperspect.a021972

Trcek T, Lehmann R. 2019. Germ granules in *Drosophila*. *Traffic* **20:** 650–660. doi:10.1111/tra.12674

Truebestein L, Leonard TA. 2016. Coiled-coils: the long and short of it. *Bioessays* **38:** 903–916. doi:10.1002/bies.2016 00062

Vaishali V, Dimitrova-Paternoga L, Haubrich K, Sun M, Ephrussi A, Hennig J. 2021. Validation and classification of RNA binding proteins identified by mRNA interactome capture. bioRxiv doi:10.1101/2021.02.02.429302

Vale RD, Reese TS, Sheetz MP. 1985. Identification of a novel force-generating protein, kinesin, involved in microtubule-based motility. *Cell* **42:** 39–50. doi:10.1016/S0092-8674(85)80099-4

Veeranan-Karmegam R, Boggupalli DP, Liu G, Gonsalvez GB. 2016. A new isoform of *Drosophila* non-muscle Tropomyosin 1 interacts with kinesin-1 and functions in oskar mRNA localization. *J Cell Sci* **129:** 4252–4264.

Williams LS, Ganguly S, Loiseau P, Ng BF, Palacios IM. 2014. The auto-inhibitory domain and ATP-independent microtubule-binding region of kinesin heavy chain are major functional domains for transport in the *Drosophila* germline. *Development* **141:** 176–186. doi:10.1242/dev.097592

Zimyanin VL, Belaya K, Pecreaux J, Gilchrist MJ, Clark A, Davis I, St Johnston D. 2008. In vivo imaging of oskar mRNA transport reveals the mechanism of posterior localization. *Cell* **134:** 843–853. doi:10.1016/j.cell.2008.06.053